ChemPubSoc Europe

DOI: 10.1002/cssc.201701757

CHEMSUSCHEM Full Papers

A Functional Hydrogenase Mimic Chemisorbed onto Fluorine-Doped Tin Oxide Electrodes: A Strategy towards Water Splitting Devices

Riccardo Zaffaroni, Remko J. Detz, Jarl Ivar van der Vlugt, and Joost N. H. Reek*[a]

A diiron benzenedithiolate hydrogen-evolving catalyst immobilized onto fluorine-doped tin oxide (FTO) electrodes is prepared, characterized, and studied in the context of the development of water splitting devices based on molecular components. FTO was chosen as the preferred electrode material owing to its conductive properties and electrochemical stability. An FTO nanocrystalline layer is also used to greatly improve the surface area of commercially available FTO while preserving the properties of the material. Electrodes bearing a covalently anchored diiron catalyst are shown to be competent for electrocatalytic hydrogen evolution from acidic aqueous media at relatively low overpotential (500 mV) with a faradaic efficiency close to unity. Compared with bulk solution catalysts, the catalyst immobilized onto the electrode surface operates at roughly 160 mV lower overpotentials, yet with similar rates.

Introduction

The development of devices for the direct conversion of solar energy into fuels is attracting much attention as a prominent solution for sustainable energy storage and supply.[1,2] Of particular interest is light-driven "splitting" of water into hydrogen and oxygen by using efficient catalysts.[3,4] Regarding the generation of hydrogen from protons and electrons, platinum is still the most efficient catalyst because it operates at high rates and very low overpotential.[5] However, the high cost and low abundance of this noble metal make application of Pt-based systems unattractive on the large scale. However, nature provides superb examples of hydrogen-evolving catalysts based on non-noble metals. Hydrogenases, metalloenzymes that utilize iron, diiron or iron–nickel as metallic components, are able to perform reversible proton reduction at ambient temperature and pressure with activities, efficiencies, and overpotentials that are comparable to platinum.[6–10] It is thus not surprising that chemists take inspiration from nature to mimic the active site of these metalloenzymes to develop new classes of proton reduction catalysts.[11–27] Although several hundreds of hydrogenase model systems have been reported to date, most have been studied as homogeneous catalysts in organic solvents.[28,29] Strategies to afford robust immobilization on conductive electrode surfaces, which are key for the development of devices, are relatively limited. The potential and advantages of immobilizing molecular catalysts have already been illustrated for cobalt-[30–40] and nickel-based catalysts,[41–44] which have been anchored onto various materials through their organic ligand structure.[45] Heterogenization of molecular diiron hydrogenase models onto supporting matrices, including metal–organic frameworks,[46] molecular sieves,[47] hydrogels,[48] or polymers,[49] has been shown to be beneficial for the activity and stability of the catalytic centers.

Preparation of electrodes decorated with hydrogenase model complexes has been reported, although hydrogen evolution studies with these modified electrodes have met with limited success.[50,51] In 2005, Vijaikanth et al. reported the immobilization of a succinimide ester-appended hydrogenase functional mimic that was attached onto amine- or aminophenyl-functionalized glassy carbon electrodes.[52] The electrode surfaces were exhaustively characterized by voltammetric measurements in organic solvents but featureless voltammograms were obtained in the presence of acid. In 2007, Darensbourg and co-workers reported a similar system based on a propanedithiolate bridged diiron complex featuring a carboxylic acid moiety for grafting onto an aniline-functionalized, highly ordered pyrolytic graphite electrode.[53] Although the immobilization was successful, the reductive electrochemical response did not persist over repeated scans, the reason being the irreversible reduction of the complex employed. Artero and co-workers reported a diiron complex containing a modified propanedithiolate bridge featuring a succinimide ester anchored onto amine-functionalized carbon and gold electrodes.[54] No hydrogen evolution was observed from these electrodes owing to deactivation of the iron catalyst in the presence of strong acids. However, the stability of the amide bond under the applied highly reductive and acidic conditions was demonstrated by immobilization of ferrocene moieties by the

[a] Dr. R. Zaffaroni, Dr. R. J. Detz, Dr. J. I. van der Vlugt, Prof. Dr. J. N. H. Reek
Van't Hoff Institute for Molecular Sciences, University of Amsterdam
Science Park 904, 1098 XH Amsterdam (The Netherlands)
E-mail: J.N.H.Reek@uva.nl

Supporting Information and the ORCID identification number(s) for the author(s) of this article can be found under: https://doi.org/10.1002/cssc.201701757.

© 2017 The Authors. Published by Wiley-VCH Verlag GmbH & Co. KGaA. This is an open access article under the terms of the Creative Commons Attribution Non-Commercial License, which permits use, distribution and reproduction in any medium, provided the original work is properly cited and is not used for commercial purposes.

same strategy. In 2016, a NiO-modified electrode functionalized with a diiron catalyst was shown to evolve hydrogen in a photocatalytic fashion.[51] In recent years, diiron model complexes featuring benzenedithiolate bridges have become increasingly popular as they impart interesting tunable electronic properties to the hydrogenase models.[11,23,27,55,56] In particular, these complexes display a mild two-electron reduction potential that is also electrochemically fully reversible, which is a key aspect for catalyst stability. The proton reduction mechanism and thus the catalytic reduction potential can be varied by utilizing acids of different strength. Most importantly, proton reduction catalysis in an acidic aqueous environment occurs already at the first reduction wave for these species.[22,57,58] For these reasons, we envisioned that immobilization of a diiron benzenedithiolate proton reduction catalyst that offers reversible electrochemical reduction behavior at mild potentials is a valuable approach for the development of electrodes decorated with molecular catalysts able to evolve hydrogen from an aqueous environment. We herein describe the preparation and electrochemical characterization of the molecular catalyst **7** (bis-ester derivative) and **8** (bis-carboxylic acid derivative), and its immobilization onto conductive fluorine-doped tin oxide (FTO) electrodes and FTO nanocrystal-modified electrodes and we report electrodes decorated with synthetic molecular diiron hydrogenase models that evolve dihydrogen gas in an aqueous pH 3.5 sulfate buffer solution, at about 500 mV overpotential, with current densities of 1.6 mA cm^{-2} and Faradaic efficiencies close to unity, as depicted in Figure 1. Hydrogen formation was confirmed and quantified by GC analysis. Furthermore, comparison of the catalytic performance of the molecular system in organic solvents to the immobilized catalyst in aqueous media reveals that the immobilized catalyst operates at similar rates yet at about 160 mV lower operational overpotential. These results highlight the importance of further development of the immobilization of diiron proton reduction catalysts and the study of their performance in aqueous environments.

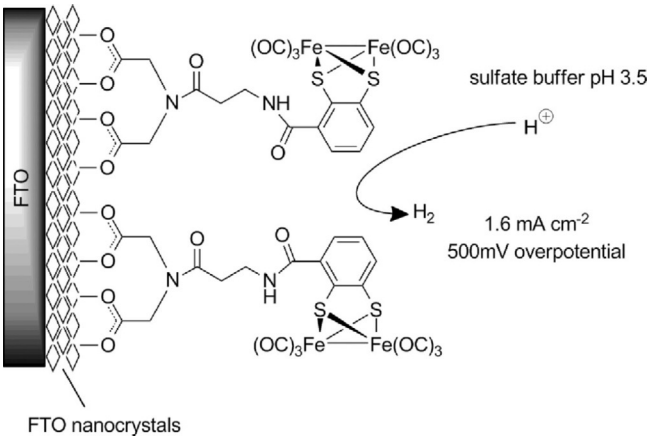

Figure 1. Schematic representation of the glass-coated FTO electrodes modified with FTO nanocrystals, decorated with molecular catalyst **8**. The electrodes display full competence for hydrogen evolution in a pH 3.5 sulfate buffer solution at 500 mV overpotential, reaching current densities up to 1.6 mA cm^{-2} and Faradaic efficiency close to unity.

Results and Discussion

The benzenedithiolate bridge allows for synthetic modifications that enable introduction of targeted functional groups to be used for immobilization of the complex on surfaces. Carboxylic acids, widely used functional groups for immobilization on metal oxide materials, provide an effective strategy to decorate electrodes with molecular catalysts. However, monocarboxylic acids may bind too weakly to metal oxides, especially at basic pH values. Therefore, a suitable linker featuring a chelating bis-carboxylic acid moiety, anticipated to bind more strongly to metal oxides, was installed on the benzenedithiolate bridge to obtain the functional diiron complex **8**. The electrode material of choice for this investigation was commercially available glass-coated FTO, as this material offers a conductive metal oxide surface with a wide electrochemical stability range, even in aqueous environments.[59] A drawback of this type of material is the relatively small surface area as a result of the intrinsic flat profile of the exposed outer layer. To overcome this limitation, FTO nanocrystals were prepared according to a modified literature procedure[60] and, for the first time, deposited onto the commercially available FTO electrodes by spin-coating, to obtain high surface area electrodes of the same material. Herein, the preparation and detailed studies of the diester molecular catalyst in homogeneous solution, as well as its bis-carboxylic acid analog **8** are presented. Subsequently, immobilization of **8** onto (nanocrystal-modified) FTO electrodes and their characterization are described. Finally, the competence of the prepared electrodes for catalytic proton reduction in acidic aqueous media is discussed.

Synthesis and characterization of complexes

Scheme 1 shows the synthetic route for the preparation of the desired diiron complex **8** from synthon **4**. Complex **4** was isolated by Ott and co-workers as a byproduct of the synthesis of the dicarboxylic acid derivative [Fe$_2$(dcbdt)(CO)$_6$] (2,6-dicarbox-

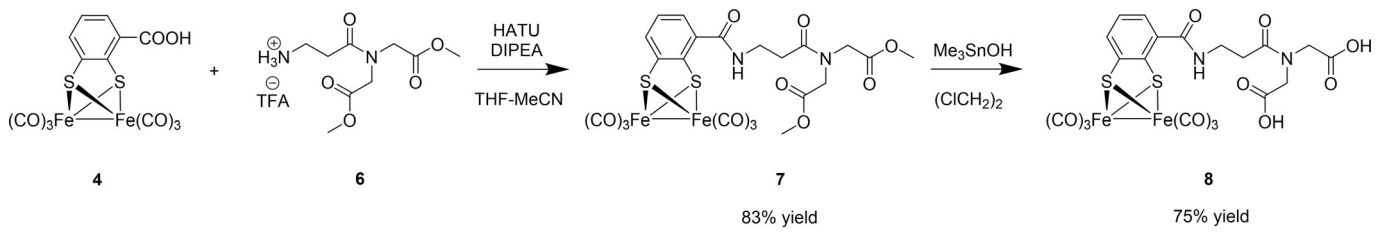

4 **6** **7** 83% yield **8** 75% yield

Scheme 1. Synthetic route for the preparation of complexes **7** and **8** from synthon **4**, Fe$_2$(mcbdt)(CO)$_6$, and linker **6**.

© 2018 The Authors. Published by Wiley-VCH Verlag GmbH & Co. KGaA, Weinheim

ylic-acid-1,2-benzodithiolate).[46,61] To date, neither detailed synthesis nor full characterization of **4** have been reported to our knowledge. We therefore include herein a convenient and scalable synthetic route, starting with the nucleophilic aromatic substitution of 1,2-dichlorobenzene by using an isopropylthiolate salt to cleanly and quantitatively afford diisopropylbenzene thioester. The reaction time of 5 days at 90 °C ensures quantitative disubstitution, avoiding inconvenient chromatography or vacuum distillation steps. Selective mono-*ortho*-lithiation with *n*-butyllithium and subsequent quenching of the lithio derivative with CO_2 yielded the carboxylic acid derivative **2**. Deprotection of both thioether groups was achieved by using sodium naphthalenide and subsequent addition of concentrated HCl to the crude reaction mixture gave access to benzenedithiol monocarboxylic acid **3**. Finally, complex **4** was prepared in 39% yield from an equimolar reaction of the iron precursor $Fe_3(CO)_{12}$ and **3**. Intermediate **5** was isolated in quantitative yield from the HATU-mediated coupling reaction of dimethyl iminodiacetate and *N*-Boc protected β-alanine (HATU = 1-[bis(dimethylamino)methylene]-1*H*-1,2,3-triazolo[4,5-*b*]pyridinium 3-oxide hexafluorophosphate, Boc = *tert*-butyloxycarbonyl). The Boc protecting group was easily removed by reaction with a 20 vol% solution of trifluoroacetic acid in dichloromethane to provide **6**. Linker **6** was used directly for HATU-assisted coupling to diiron compound **4**. This coupling reaction was performed in THF/MeCN at room temperature in the presence of 5 equivalents of *N*,*N*-diisopropylethylamine (DIPEA). The reaction was finished after 30 min (monitored by thin-layer chromatography) and work-up afforded compound **7** in 83% yield. Methyl ester deprotection employing common saponification methods proved to be problematic as decomposition of the diiron core was observed, likely as a result of irreversible binding of the generated carboxylates to the iron centers. The ester hydrolysis was successfully achieved by treating **7** with an excess of the very mild deprotecting agent trimethyltin hydroxide (Me_3SnOH), affording the desired complex **8** in 75% yield.[62]

Figure 2 shows the solid-state structure of **8** obtained by single-crystal X-ray diffraction, the crystals for which were grown by layering a THF solution of **8** with hexanes at 4 °C. The complex displays the typical butterfly configuration with each iron atom in a distorted octahedral geometry. Although the linker extends towards the diiron core, coordination of the carboxylic acids to the metal centers is not observed in the solid state. The relevant distances and angles are in agreement with literature values for similar hexacarbonyl diiron complexes.[56]

Cyclic voltammetry studies in homogeneous solution

Voltammetric studies of complex **7**, the diester analog of the dicarboxylic acid **8**, are described first to understand the main electrochemical properties of this class of substituted benzenedithiolate derivatives. Cyclic voltammograms of **7** in THF display one Nerstian reversible reduction at −1.33 V versus Fc/Fc^+ (ferrocene/ferrocenium; Figure S5 in the Supporting Information). Application of the iso-point method[63] and bulk electrolysis at constant potential (−1.75 V vs. Fc/Fc^+) indicate a two-electron process (Figure S8). Interestingly, the reduction potential of **7** is about 75 mV higher than the parent unfunctionalized benzenedithiolate complex. This effect is attributed to the electron-withdrawing character of the carbonyl substituent on the benzenedithiolate bridge.

The electrochemical behavior of **7** in THF in the presence of acid was investigated by adding various acids with different strengths whilst monitoring the reduction peak. When acetic acid ($pK_a = 23.5$ in MeCN) or benzoic acid ($pK_a = 21.5$ in MeCN) was added, the shape and position of the reductive peak did not change. In contrast, Figure 3 shows the voltammetric response obtained when increasing amounts of chloroacetic acid ($pK_a = 18.8$ in MeCN) were added, with the reductive peak shifting to less negative potentials while the current of the backward oxidative peak progressively decreases. This trend is consistent with protonation at the iron–iron bond. In agreement with this, the newly formed bridging hydride undergoes re-oxi-

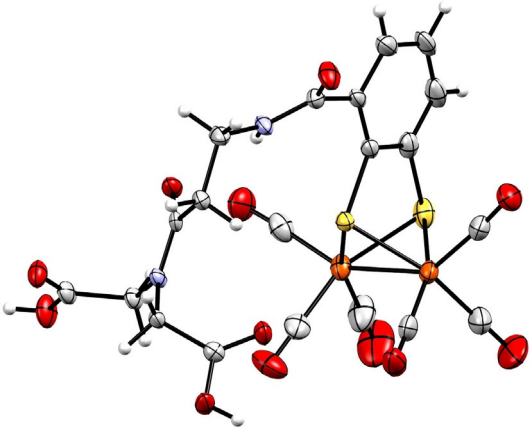

Figure 2. X-ray crystal structure of complex **8**. Thermal ellipsoids are set at 50% probability. Water crystallization molecule is omitted for clarity. Selected distances: Fe–Fe 2.4967(8), Fe–S average 2.263 ± 0.005, Fe–CO average 1.799 ± 0.013 Å.

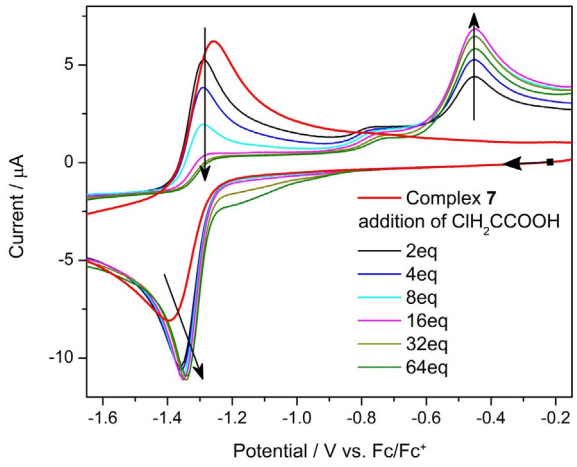

Figure 3. Voltammetric response of a THF solution of **7** in the presence of increasing amounts of chloroacetic acid.

 © 2018 The Authors. Published by Wiley-VCH Verlag GmbH & Co. KGaA, Weinheim

dation around −0.45 V versus Fc/Fc^+. The progressive anodic shifting of the peak potential when increasing aliquots of acid are added indicates that transfer of a proton is part of the electrochemical event. Peak potential analysis[64] was applied to obtain information about the number of protons involved in this step, having already established that the reduction event is a two-electron process, as the intensity of the reductive peak in the presence of acid is similar to that of the complex in absence of substrate (H^+). This analysis relates the variation of the peak potential with the acid concentration [Eq. (S1)]. The data indicate a one-proton event, as suggested by the 10.5 mV slope obtained (theoretical value = 12.5 mV; Figure S9).

Increasing the potential window to more reductive potentials results in the appearance of a catalytic proton reduction peak at around −2.05 V versus Fc/Fc^+ (Figure S10). This event corresponds to the reduction of the previously generated bridging hydride and its subsequent protonation that is associated with hydrogen release. The catalytic mechanism for proton reduction follows an (E)ECEC mechanism, similar as for previously reported hexacarbonyl benzenedithiolate diiron complexes, suggesting that modification of the bridge does not significantly affect the electronic properties of the complex. Although **7** has a milder first reduction potential compared with the unfunctionalized benzenedithiolate derivative, both complexes show catalysis at very similar redox potentials. The milder first reduction potential of **7** could be relevant in aqueous media where the complex is expected to show catalysis at its first reduction potential.[22,55,57]

The redox behavior of **8** in THF is rather peculiar, unique, and very different to that of **7**. When a small potential window is investigated—in the absence of external chloroacetic acid—the reductive scan displays a non-reversible reduction wave at −1.31 V versus Fc/Fc^+ (Figure 4, left). Interestingly, a re-oxidation wave is also present around −0.45 V versus Fc/Fc^+, consistent with the re-oxidation of the bridging hydride, as observed for **7** in the presence of acid. The electrochemical process can be summarized as a two-electron reduction followed by intramolecular protonation of the iron–iron bond by a carboxylic acid group present on the linker strap (Scheme 2, top half). This protonation step is relatively fast, as indicated by complete loss of reversibility at all scan rates. In comparison, about 16 equivalents of chloroacetic acid are needed to achieve full protonation of complex **7** in its doubly reduced state (Figure 3). This gives a rough estimation of the pK_{a1} of the internal acid groups, which must be lower than that of chloroacetic acid.

Figure 4 (right) shows that when the scan window is increased to more reductive potentials, a second irreversible wave is observed at −2.05 V, at the potential where **7** displays proton reduction. After the two-electron reduction event and intramolecular proton transfer, the bridging hydride formed is reduced at −2.05 V and a second proton from the linker is transferred to the iron–iron core, resulting in stoichiometric hydrogen evolution. The second proton transfer appears considerably slower than the first one, as the feature assigned to the re-oxidation of the bridging hydride is still evident around −0.45 V, placing pK_{a2}, relative to the second proton transfer from acidic group on the linker, at values roughly comparable to or higher than that of chloroacetic acid. After hydrogen evolution, a mono-reduced Fe^0–Fe^I diiron species is generated with dicarboxylate functional side-arms ($[\mathbf{8}(COO)_2]^{3-}$). This species, overall tri-anionic, can be mono-oxidized at −1.30 V versus Fc/Fc^+, resulting in a di-anionic Fe^I–Fe^I species, as indicated by the quasi-reversible first reduction wave along the back-oxidation trace. This wave is approximately half of the intensity of the forward first reduction of complex **8**. The processes described are depicted in Scheme 2. Next, we studied the electrochemistry of **8** in the presence of acid. Addition of increasing aliquots of chloroacetic acid confirms the presence of the catalytic wave at −2.05 V, consistent with hydrogen evolution (Figure S12); this is the same potential as where **7** displays catalysis. The carboxylic acid groups present on the linker of complex **8**, which act as proton relays, preorganizing the substrates (H^+) for proton reduction. Proton preorganization around the catalyst is expected to have a clear effect on the performance of the catalyst. The next section briefly dis-

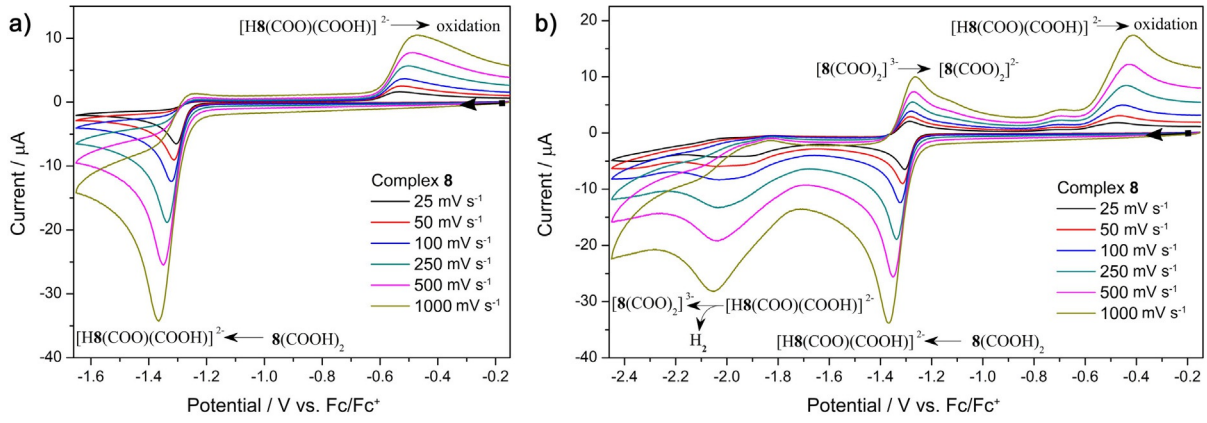

Figure 4. a) Voltammetric response for a THF solution of **8** at different scan speeds—in the absence of external chloroacetic acid—including only the first reduction event. b) Voltammetric response for a THF solution of **8** at different scan speeds—in the absence of external chloroacetic acid—including the second reduction and stoichiometric hydrogen evolution.

© 2018 The Authors. Published by Wiley-VCH Verlag GmbH & Co. KGaA, Weinheim

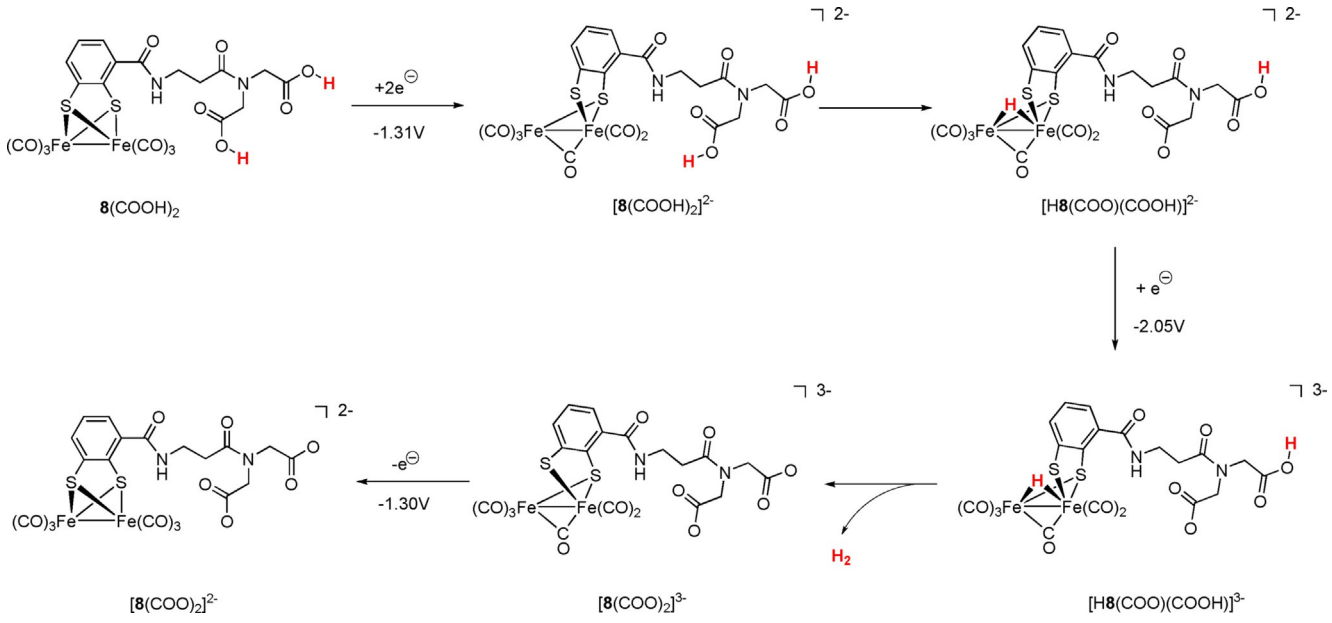

Scheme 2. Summary of the processes involved during a voltammetric scan of a THF solution of **8**—in the absence of external chloroacetic acid—featuring the evolution of stoichiometric amounts of hydrogen.

cusses the catalytic proton reduction rates for complexes **7** and **8** under identical conditions.

Foot-of-the-wave analysis in organic solvent

Plateau currents, necessary to determine catalytic rates, were not experimentally reached. Foot-of-the-wave analysis (FotW)[65] was therefore performed to access the catalytic rate constants for **7** and **8**. The slopes of the curves thus obtained can be used to obtain the catalytic rate constants (k_{cat}) under defined conditions. Figure 5 reveals the role of the internal (carboxylic acid) proton relays by a comparison of the FotW curves obtained for **7** and **8** under catalytic conditions. The curve for **7** presents a constant slope, indicating that the catalyst operates at the same rate from the catalytic onset potential ($\xi=0$) to the catalytic half-wave potential ($\xi=0.5$). Substrate depletion or catalyst decomposition are not observed. The corresponding FotW curve for catalyst **8** instead shows a steep rise, followed by a second regime that is similar to that of **7**. This accelerating effect is attributed to the presence of the internal carboxylic acids, which are associated with a faster intramolecular proton transfer relative to the intermolecular protonation events involving the external acid. Furthermore, this apparent acceleration effect only occurs for a couple of turnovers (as indicated by $I_p/I_p^0 \approx 5$; according to the proposed (E)ECEC mechanism, one-electron activation step and two electrons per catalytic cycle). When the internal acidic protons are depleted, **8** operates at similar rates as **7**. The FotW curve for **8** also gives some insights concerning catalyst decomposition, likely arising from the irreversible coordination of the carboxylate groups to the diiron core of the complex, as indicated by the decrease in the second slope for complex **8** around $\xi=$ 0.35. For each of the three slopes noted in Figure 5, the cata-

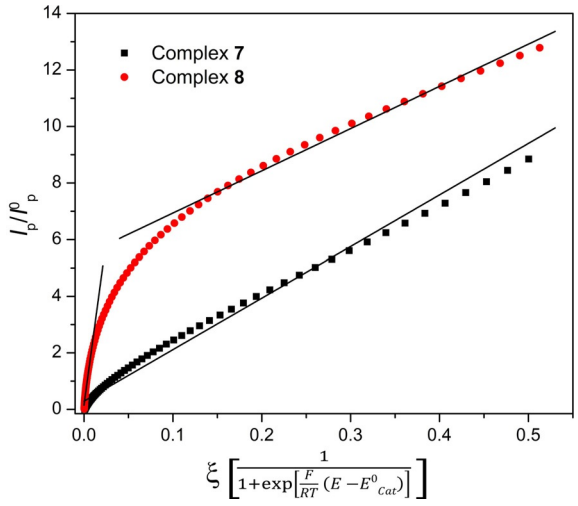

Figure 5. Foot-of-the-wave curves for **7** and **8** for voltammograms recorded at 0.1 Vs^{-1} in the presence of 64 equivalents of chloroacetic acid. FotW analysis is shown only for one scan rate for clarity reasons, but the slopes indicated are obtained from a dataset with six different scan rates.

Table 1. Summary of the relevant catalytic parameters for complexes **7** and **8** obtained by FotW analysis. TOF_{max} is calculated for 1 M concentration of substrate. The overpotential reported is valid under the assumption that the thermodynamic proton reduction potential of the acid used (chloroacetic acid) is equal in acetonitrile and THF.

Parameter	Complex **7**	Complex **8**	
	main domain	first acceleration	main domain
k_{cat} [$M^{-1}s^{-1}$]	2.25×10^3	3.25×10^5	2.25×10^3
TOF_{max} [s^{-1}]	4.5×10^3	6.5×10^5	4.5×10^3
catalytic $E_{1/2}$ potential [V vs. Fc/Fc^+]	−1.93	−1.95	−1.93
Overpotential [V]	0.66	0.68	0.66

© 2018 The Authors. Published by Wiley-VCH Verlag GmbH & Co. KGaA, Weinheim

lytic rate constant k_{cat}, summarized in Table 1, can be calculated. The catalytic performances of the two complexes are nearly identical. The main difference is the proton preorganization around **8**, which is responsible for the initial acceleration effect. The data suggest that during a catalytic cycle with intact carboxylic acid groups in **8**, only the first protonation happens intramolecularly from the acidic protons on the linker. The second one, associated with hydrogen evolution, likely involves proton transfer from the external acid in solution. This is indicated by the studies in the absence of acid, which suggest that the second protonation by the internal carboxylic acid is slow compared with the first proton transfer event. After the second catalytic cycle and depletion of the acidic protons on the linker, which cannot be quickly replenished by chloroacetic acid as this acid has similar or lower strength, **8** operates at similar rates to **7**. This indicates that a catalyst appended with proton relays that can be re-protonated by an external acid at rates faster than catalytic rates could result in increased catalytic activity whilst keeping the overpotential unaffected.

Electrode preparation and catalyst immobilization

Immobilization of the molecular catalyst **8** is performed on both commercially available glass-coated FTO electrodes and on self-fabricated high surface area FTO nanocrystals modified electrodes. The high surface area FTO electrodes were prepared by attachment of a layer of FTO nanocrystals to flat commercial glass-coated FTO. A known amount of FTO nanocrystals, prepared according to a modified literature procedure,[60] was suspended in formic acid and ground with a mortar and pestle for 15 min. After this, the solids were used to prepare a 30 mol% suspension in neat formic acid. This suspension was sonicated for 30 min whereafter it was used to spin-coat clean FTO electrodes. The slides were then placed in a furnace oven; the temperature was increased to 500 °C over 3 h, the samples were kept at this temperature for 30 min and then allowed to cool to room temperature. SEM measurements of the high surface area FTO electrodes display a 10–30 nm homogeneous distribution of the particle size of the FTO nanocrystals (Figure S17). The particle size is consistent with the value calculated from the XRD data by using the Scherrer equation (Figure S19).

Immobilization of compound **8** was achieved by submerging the electrodes (after heat treatment at 120 °C for 30 min) in a 0.5 mM catalyst solution in THF overnight. Subsequently, the electrodes were thoroughly washed with THF to remove any unbound catalyst, dried with a stream of argon, and used directly for the measurements. Figure 6 shows the attenuated total reflectance (ATR) FTIR spectrum of the functionalized electrodes displaying the characteristic signature of iron-bound CO ligands ($\nu = 2076$, 2040, 2004 cm^{-1}) and the organic carbonyl peaks ($\nu = 1739$ and 1641 cm^{-1})—only minor shifts are observed with respect to the parent compound **8** in THF solution. SEM pictures of the electrodes with and without catalysts do not show evident differences, indicating that the immobilization process does not change the FTO profile. Energy-dispersive X-ray (EDX) spectroscopy of the electrodes after functionalization with catalyst demonstrated homogeneous distributions of iron and sulfur in a 1:1 ratio, whereas such elements are absent in the unfunctionalized clean electrodes.

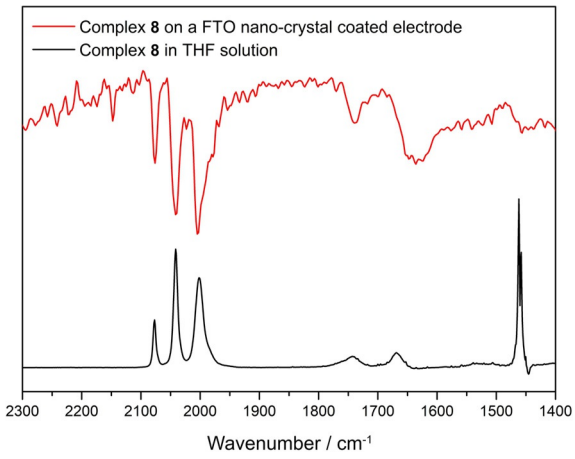

Figure 6. IR spectrum of complex **8** in THF solution (black line) and ATR FTIR spectrum of **8** immobilized on nanocrystalline FTO-coated electrode.

Electrochemical measurements of modified electrodes

It is anticipated that the redox behavior of the immobilized catalyst **8** will be comparable to the redox behavior of **7** in THF solution, as the acidic protons of the linker are absent upon chemisorption of the carboxylates to the metal oxide substrate (electrode). Two sets of data will be presented for catalyst **8** immobilized on electrodes; one on commercially available glass-coated FTO, the other for modified electrodes coated with FTO nanocrystals. As shown in Figure 7, the voltammograms feature a wave at −1.35 V versus Fc/Fc^+ consistent with the reversible two-electron reduction of the diiron complex. Although the peak potential separation is larger than expected for a species immobilized on an electrode (around 0 V for a well-behaved system with a relatively high heterogeneous rate of electron transfer k_0),[66] a plot of the peak current versus scan rate shows a linear trend, which confirms the immobilization of **8** (Figures S13 and S14). From the slopes of these lines, the catalyst loading for the different types of electrodes were estimated to be on the order of $3.3\times10^{-12}\pm8.5\times10^{-14}$ mol cm^{-2} for the flat FTO electrodes, in accordance with monolayer coverage of the electrode, whereas for the high surface area modified FTO nanocrystals coated electrodes the catalyst loading is about two orders of magnitude higher, reaching $5.3\times10^{-10}\pm9.2\times10^{-11}$ mol cm^{-2}.

For comparison, in a different set of experiments, complex **4** was also immobilized on the modified electrodes. Rapid loss of the corresponding response in cyclic voltammetry indicates that this compound does not persist at the surface after only a few cycles, suggesting that a single anchoring group close to the redox active site does not result in proper immobilization on the electrode.

© 2018 The Authors. Published by Wiley-VCH Verlag GmbH & Co. KGaA, Weinheim

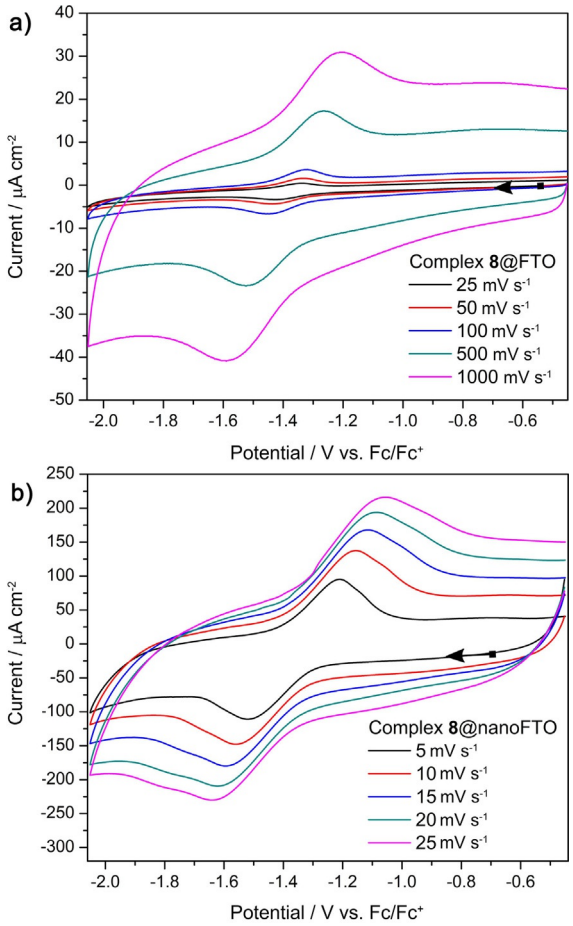

Figure 7. Voltammetric response of catalyst-functionalized electrodes measured in THF with $N(Bu)_4PF_6$ as supporting electrolyte. a) Complex **8** immobilized on flat FTO. b) Complex **8** immobilized on nanocrystalline FTO-coated electrodes.

Electrolysis at constant potential in aqueous media

The catalyst-modified electrodes were examined for hydrogen evolution at pH 3.5 by using 50 mM sulfate buffer solution as electrolyte. This pH value has been chosen as a compromise between activity of the catalyst and limited background reaction from the FTO electrodes.

The bias potential applied for the electrolysis was −0.7 V versus NHE, sufficient to access the first reduction of the complex. The electrolysis cell employed was a two-compartment cell; one containing the modified working electrode and a reference electrode, the other containing a platinum coil counter-electrode, separated from the main compartment by a glass frit. The cell was connected to a GC set-up to monitor hydrogen evolution with time. Visual inspection of the working modified electrodes under catalytic conditions revealed the formation of small hydrogen bubbles trapped at the electrode surface, particularly for the nano-FTO material.[67] Table 2 summarizes the results for the two types of electrodes described together with their respective blank control measurements.

The nanocrystalline FTO-coated electrodes, having a higher surface area, accommodate about 160 times more catalyst than the flat FTO electrodes, leading to a current density of

Table 2. Summary of the results from electrolysis experiments coupled with GC of the headspace (50 mM $NaHSO_4$ at pH 3.5 and −0.7 V bias potential vs. NHE) of complex **8** immobilized on modified FTO electrodes.

Parameter	**8**@FTO	**8**@nanocrystalline FTO
Blank electrode		
H_2 evolved [μL]	2.7	5.9
catalyst loading [mol cm^{-2}]	3.33×10^{-12} $\pm8.5\times10^{-14}$	5.29×10^{-10} $\pm9.2\times10^{-11}$
Current density [mA cm^{-2}]	0.6	1.6
Catalyst-functionalized electrode		
H_2 evolved [μL]	11.1	29.2
Faradaic efficiency [%]	95	86
TON	1.37×10^{5}	2.26×10^{3}

1.6 mA cm^{-2} at 500 mV overpotential. Interestingly, they show about two orders of magnitude lower turnover numbers (TONs). This is tentatively attributed to fast depletion of protons around the catalyst.[68] Slow diffusion of electrolyte owing to the intrinsic properties of the mesoporous substrate, associated with fast depletion of the protons, would increase the local pH around the catalyst, hampering catalyst stability and activity or causing leaching of the catalyst from the FTO surface. As observed during the deprotection of the methyl ester groups of complex **7** through traditional saponification methods, basic pH is incompatible with compound **8**. A similar conclusion can be drawn from the current density plots, Figure 8, where the relatively rapid drop in current density after a few seconds indicates depletion of substrates. After this initial phase, the current density continues to drop as a result of catalyst deactivation or catalyst leaching owing to hydrolysis of the chelating carboxylates from the metal oxide surface. Although the prepared electrodes are demonstrated to be competent in producing hydrogen, their stability under catalytic conditions remains an issue, as the electrodes are only stable for several minutes.

FotW analysis was employed to deduce the catalytic rate for proton reduction in acidic aqueous environment for the immo-

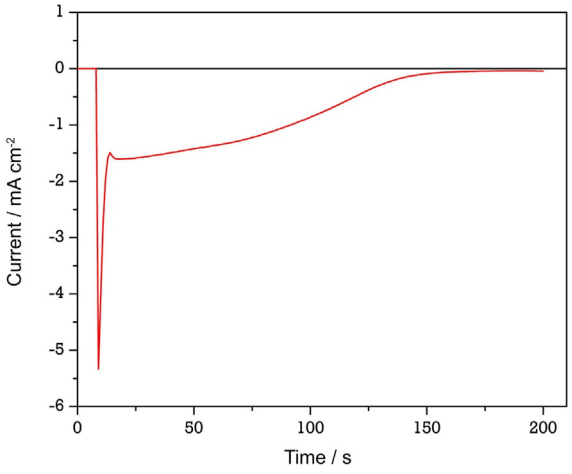

Figure 8. Current density plot for complex **8** immobilized on nanocrystalline FTO-coated electrode.

© 2018 The Authors. Published by Wiley-VCH Verlag GmbH & Co. KGaA, Weinheim

bilized catalyst on FTO electrodes. Consistent with the current density plot, it is noted that the catalytic response does not persist for several voltammetric scans. Nevertheless, this analysis for the immobilized complex **8** on flat FTO with a catalyst loading of 3.33×10^{-12} mol cm^{-2} reveals a catalytic constant k_{cat} of 5.95×10^{3} M^{-1} s^{-1}. The calculated constant is in agreement with the one calculated for the same catalyst dissolved in organic solvents in the presence of weak acid, corroborating the presence of the molecular catalyst on the FTO surface. The information from the electrocatalytic data in organic solvent and acidic aqueous media is summarized in Figure 9 in a comparative Tafel plot. This plot, although based on one measured data point (the inflection point), clearly demonstrates the advantage of immobilization, as switching from organic solvents to aqueous media results in approximately 160 mV lower overpotential and a four-fold increase in catalyst activity.

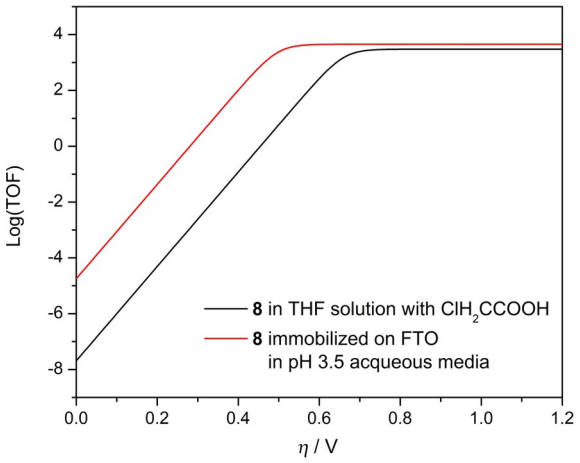

Figure 9. Comparative Tafel plot for (black) a THF solution of **8** in the presence of weak acid (chloroacetic acid) and for (red) **8** immobilized on flat FTO electrodes in aqueous media at pH 3.5. TOF_{max} is extrapolated for a 1 M substrate concentration.

Conclusions

In this work, we have not only demonstrated the immobilization of diiron benzenedithiolate complexes on conductive FTO electrodes but also shown that FTO nanocrystals can be employed to effectively increase the surface area of this material. Furthermore, the prepared electrodes are able to perform hydrogen evolution from aqueous environments at mild overpotentials. The activity of the catalyst was evaluated both in the homogeneous phase and for the heterogenized system. From the studies in organic media, it is evident that proton relays around the catalyst can greatly improve the catalytic rates of the catalyst whereas studies of the immobilized catalyst reveal that the same catalyst can operate at lower overpotentials, yet with similar rates when in acidic aqueous media. These observations could pave the way for the development of a second-generation catalyst equipped with proton relays. Such functional groups could induce important (side) effects, such as more favorable proton transfer from the "bulk" medium to the catalyst and faster electrolyte refreshing rates, functioning as a buffer. With this first generation of electrodes, high reaction rates and turnover numbers have been achieved, nevertheless the long-term stability of the catalyst-functionalized electrodes needs to be improved.

Experimental Section

General procedures

All synthetic procedures were carried out under an argon atmosphere by using standard Schlenk techniques. All commercially available chemicals were used as received without further purification. Solvents used for synthesis were dried by the most suitable method, distilled, and degassed. Column chromatography was performed open to air using solvents as received. Other experimental details can be found in the Supporting Information.

Compound 5

To a round-bottom Schlenk flask containing dimethyl iminodiacetate hydrochloride (1.5 g, 7.9 mmol, 1 equiv), *N*-Boc-β-alanine (1.72 g, 8.7 mmol, 1.1 equiv), HATU coupling agent (3.31 g, 8.7 mmol, 1.1 equiv), dry DMF (50 mL), and DIPEA (6.9 mL, 39.6 mmol, 5 equiv) were added and the mixture was stirred at room temperature overnight. The volatiles were removed under vacuum and the residue dissolved in ethyl acetate. The organic phase was washed with saturated $NaHCO_3$ (3×50 mL), 0.5 M HCl (3×50 mL), and brine (50 mL). The organic layer was dried with $MgSO_4$ and the solvent removed under vacuum to afford a red-orange oil that was purified by column chromatography on silica gel with ethyl acetate. The product can be visualized on TLC by using ninhydrin stain solution. After the solvent was evaporated, a clear oil was obtained (2.51 g, 95.5%). ^{1}H NMR (CD_2Cl_2): $\delta=5.22$ (br s, 1H), 4.18 (s, 2H), 4.17 (s, 2H), 3.78 (s, 3H), 3.74 (s, 3H), 3.41 (q, $J=6$ Hz, 2H), 2.52 (t, $J=6$ Hz, 2H), 1.44 ppm (s, 9H).

Compound 6

Trifluoroacetic acid (TFA, 5 mL) was slowly added to a CH_2Cl_2 (20 mL) solution of **5** (2 g, 6.0 mmol). The solution was stirred at room temperature for 2 h, whereafter the volatiles were removed under vacuum to afford a pale-yellow liquid. The residue was dissolved in a minimum amount of CH_2Cl_2 and toluene (150 mL) was added. All volatiles were removed under reduced pressure to afford a very hygroscopic off-white solid in quantitative yield (2.0 g), which was used without further purification. ^{1}H NMR (CD_3CN): $\delta=7.40$ (bs s, 1H), 4.21 (s, 2H), 4.15 (s, 2H), 3.74 (s, 3H), 3.70 (s, 3H), 3.21 (t, $J=6$ Hz, 2H), 3.19 ppm (t, $J=6$ Hz, 2H).

Compound 7

To an argon-flushed round-bottom Schlenk flask containing **4** (250 mg, 0,54 mmol, 1 equiv), **6** (242.5 mg, 0.70 mmol, 1.3 equiv), HATU coupling agent (266.3 mg, 0.7 mmol, 1.3 equiv), a 1:1 mixture of dry THF and dry acetonitrile (total 20 mL), and DIPEA (469 μL, 2.69 mmol, 5 equiv) were added and the mixture was stirred at room temperature. The reaction was monitored with TLC and considered finished after 30 min. The solvents were removed under vacuum and the residue dissolved in ethyl acetate (50 mL). The organic layer was washed with water (3×50 mL), saturated $NaHCO_3$ (50 mL), 0.5 M HCl (50 mL), and brine (50 mL). The organic layer was dried with $MgSO_4$, filtered, and the solvent removed under

© 2018 The Authors. Published by Wiley-VCH Verlag GmbH & Co. KGaA, Weinheim

vacuum to afford a red solid, which was purified by column chromatography on silica gel with ethylacetate/NEt_3 99:1 to afford a red solid (312 mg, 83.3% yield). ^{1}H NMR (CD_2Cl_2): δ = 7.26 (d, J = 7.8 Hz, 1H), 6.93 (d, J = 7.8 Hz, 1H), 6.90 (br t, J = 6 Hz, 1H), 6.74 (t, J = 7.4 Hz, 1H), 4.19 (s, 2H), 4.17 (s, 2H), 3.77 (s, 3H), 3.74 (s, 3H), 3.70 (q, J = 6.0 Hz, 2H), 2.64 ppm (t, J = 6.0 Hz, 2H); FTIR (THF): $\tilde{\nu}$ = 2075, 2038, 2003 cm^{-1}; HR-MS (CSI, pos.): m/z calcd for $C_{22}H_{19}Fe_2N_2O_{12}S_2$ ($M+H^+$): 678.9077; found: 678.9086; calcd for $C_{22}H_{19}Fe_2N_2NaO_{12}S_2$ ($M+Na^+$): 700.8899; found: 700.8902.

Compound 8

To an argon-flushed round-bottom Schlenk flask containing compound **7** (260 mg, 0.37 mmol, 1 equiv) and trimethyltin hydroxide (676 mg, 3.7 mmol, 10 equiv), 1,2-dichloroethane was added (10 mL) and the solution was heated at 80 °C for 3 h. After cooling the solution to room temperature, ethyl acetate was added and the organic phase was washed with 1 M HCl (3×50 mL) and brine (50 mL), dried with $MgSO_4$, and the solvent removed under vacuum to afford an orange solid. The solid was dissolved in CH_2Cl_2 and precipitated by addition of hexanes (187 mg, 75% yield). ^{1}H NMR (CD_2Cl_2): δ = 7.28 (d, J = 7.8 Hz, 1H), 7.02 (br t, J = 6 Hz, 1H), 6.91 (d, J = 7.8 Hz, 1H), 6.76 (t, J = 7.4 Hz, 1H), 4.23 (s, 2H), 4.16 (s, 2H), 3.71 (q, J = 6.0 Hz, 2H), 2.67 ppm (t, J = 6.0 Hz, 2H); FTIR (THF): $\tilde{\nu}$ = 2076, 2040, 2004, 1739, 1641 cm^{-1}; HR-MS (CSI, neg.): m/z calcd for $C_{20}H_{13}Fe_2N_2O_{12}S_2$ ($M-H^+$): 648.8610; found: 648.8893.

FTO nanocrystals

FTO nanocrystals were prepared according to a modified literature procedure.[60] Tin tetrachloride (1.5 mL) was slowly added to a Teflon beaker containing water (30 mL). After stirring this solution for 5 min, HF (50% solution in water, 0.5 mL) was added. Concentrated ammonia was added to the solution dropwise until a sol-gel was obtained and the pH of the liquid became basic. The sol-gel was dried at 100 °C in an oil-bath overnight. The resulting solid was triturated in a mortar and calcined at 500 °C for 30 min. The powder obtained was further ground in a mortar. XRD powder diffraction: 2θ = 26.5, 33.8, 37.8, 51.7, 54.6, and 55.5°. A lower indication of the crystallites particle size can be obtained from the Scherrer equation by measuring the width of the peaks at half-height. The mean particle size is estimated to be around 6 nm.

Acknowledgements

*This work is part of the research program of the Foundation for Fundamental Research on Matter (FOM), which is part of the Netherlands Organization for Scientific Research (NWO). Dr. Wojciech I. Dzik is acknowledged for X-ray data collection and refinement of the crystal structure. Dr. Erik Garnett is acknowledged for SEM data collection. René Becker is acknowledged for devising the synthetic route for complex **4**.*

Conflict of interest

The authors declare no conflict of interest.

Keywords: hydrogenases · electrocatalysis · electrodes · immobilization · water splitting

[1] Y. Amao, *ChemCatChem* **2011**, *3*, 458 – 474.
[2] N. S. Lewis, D. G. Nocera, *Proc. Natl. Acad. Sci. USA* **2006**, *103*, 15729 – 15735.
[3] T. Bak, J. Nowotny, M. Rekas, C. C. Sorrell, *Int. J. Hydrogen Energy* **2002**, *27*, 991 – 1022.
[4] R. M. Bullock, A. M. Appel, M. L. Helm, *Chem. Commun.* **2014**, *50*, 3125 – 3143.
[5] M. Carmo, D. L. Fritz, J. Merge, D. Stolten, *Int. J. Hydrogen Energy* **2013**, *38*, 4901 – 4934.
[6] W. Lubitz, H. Ogata, O. Rudiger, E. Reijerse, *Chem. Rev.* **2014**, *114*, 4081 – 4148.
[7] P. Knörzer, A. Silakov, C. E. Foster, F. A. Armstrong, W. Lubitz, T. Happe, *J. Biol. Chem.* **2012**, *287*, 1489 – 1499.
[8] F. A. Armstrong, *Curr. Opin. Chem. Biol.* **2004**, *8*, 133 – 140.
[9] E. M. Shepard, F. Mus, J. N. Betz, A. S. Byer, B. R. Duffus, J. W. Peters, J. B. Broderick, *Biochemistry* **2014**, *53*, 4090 – 4104.
[10] J. W. Peters, G. J. Schut, E. S. Boyd, D. W. Mulder, E. M. Shepard, J. B. Broderick, P. W. King, M. W. Adams, *Biochim. Biophys. Acta Mol. Cell Res.* **2015**, *1853*, 1350 – 1369.
[11] G. A. N. Felton, A. K. Vannucci, J. Chen, L. T. Lockett, N. Okumura, B. J. Petro, U. I. Zakai, D. H. Evans, R. S. Glass, D. L. Lichtenberger, *J. Am. Chem. Soc.* **2007**, *129*, 12521 – 12530.
[12] M. Wang, L. Chen, L. C. Sun, *Energy Environ. Sci.* **2012**, *5*, 6763 – 6778.
[13] L. Schwartz, P. S. Singh, L. Eriksson, R. Lomoth, S. Ott, *C. R. Chim.* **2008**, *11*, 875 – 889.
[14] I. K. Pandey, S. M. Mobin, N. Deibel, B. Sarkar, S. Kaur-Ghumaan, *Eur. J. Inorg. Chem.* **2015**, 2875 – 2882.
[15] X. Wang, T. Y. Zhang, Q. S. Yang, S. Jiang, B. Li, *Eur. J. Inorg. Chem.* **2015**, 817 – 825.
[16] L. C. Song, C. G. Li, J. Gao, B. S. Yin, X. Luo, X. G. Zhang, H. L. Bao, Q. M. Hu, *Inorg. Chem.* **2008**, *47*, 4545 – 4553.
[17] G. Durgaprasad, R. Bolligarla, S. K. Das, *J. Organomet. Chem.* **2011**, *696*, 3097 – 3105.
[18] M. E. Carroll, B. E. Barton, T. B. Rauchfuss, P. J. Carroll, *J. Am. Chem. Soc.* **2012**, *134*, 18843 – 18852.
[19] R. Zaffaroni, T. B. Rauchfuss, D. L. Gray, L. De Gioia, G. Zampella, *J. Am. Chem. Soc.* **2012**, *134*, 19260 – 19269.
[20] J. M. Camara, T. B. Rauchfuss, *Nat. Chem.* **2012**, *4*, 26 – 30.
[21] J. C. Lansing, J. M. Camara, D. E. Gray, T. B. Rauchfuss, *Organometallics* **2014**, *33*, 5897 – 5906.
[22] R. Becker, S. Amirjalayer, P. Li, S. Woutersen, J. N. Reek, *Sci. Adv.* **2016**, *2*, e1501014.
[23] S. Ezzaher, A. Gogoll, C. Bruhn, S. Ott, *Chem. Commun.* **2010**, *46*, 5775 – 5777.
[24] S. Ezzaher, P. Y. Orain, J. F. Capon, F. Gloaguen, F. Y. Petillon, T. Roisnel, P. Schollhammer, J. Talarmin, *Chem. Commun.* **2008**, 2547 – 2549.
[25] L.-C. Song, L.-X. Wang, B.-S. Yin, Y.-L. Li, X.-G. Zhang, Y.-W. Zhang, X. Luo, Q.-M. Hu, *Eur. J. Inorg. Chem.* **2008**, 291 – 297.
[26] L. Duan, M. Wang, P. Li, N. Wang, F. Wang, L. Sun, *Inorg. Chim. Acta* **2009**, *362*, 372 – 376.
[27] J. Chen, A. K. Vannucci, C. A. Mebi, N. Okumura, S. C. Borowski, M. Swenson, L. T. Lockett, D. H. Evans, R. S. Glass, D. L. Lichtenberger, *Organometallics* **2010**, *29*, 5330 – 5340.
[28] Y. Li, T. B. Rauchfuss, *Chem. Rev.* **2016**, *116*, 7043 – 7077.
[29] D. Schilter, J. M. Camara, M. T. Huynh, S. Hammes-Schiffer, T. B. Rauchfuss, *Chem. Rev.* **2016**, *116*, 8693 – 8749.
[30] R. M. Kellett, T. G. Spiro, *Inorg. Chem.* **1985**, *24*, 2378 – 2382.
[31] F. Zhao, J. Zhang, T. Abe, D. Wöhrle, M. Kaneko, *J. Mol. Catal. A* **1999**, *145*, 245 – 256.
[32] L. A. Berben, J. C. Peters, *Chem. Commun.* **2010**, *46*, 398 – 400.
[33] F. Lakadamyali, A. Reynal, M. Kato, J. R. Durrant, E. Reisner, *Chem. Eur. J.* **2012**, *18*, 15464 – 15475.
[34] N. M. Muresan, J. Willkomm, D. Mersch, Y. Vaynzof, E. Reisner, *Angew. Chem. Int. Ed.* **2012**, *51*, 12749 – 12753; *Angew. Chem.* **2012**, *124*, 12921 – 12925.

 © 2018 The Authors. Published by Wiley-VCH Verlag GmbH & Co. KGaA, Weinheim

[35] A. Reynal, F. Lakadamyali, M. A. Gross, E. Reisner, J. R. Durrant, *Energy Environ. Sci.* **2013**, *6*, 3291 – 3300.
[36] X. J. Chen, H. Ren, W. Peng, H. M. Zhang, J. T. Lu, L. Zhuang, *J. Phys. Chem. C* **2014**, *118*, 20791 – 20798.
[37] N. Kaeffer, A. Morozan, V. Artero, *J. Phys. Chem. B* **2015**, *119*, 13707 – 13713.
[38] C. Bachmann, B. Probst, M. Oberholzer, T. Fox, R. Alberto, *Chem. Sci.* **2016**, *7*, 436 – 445.
[39] J. Willkomm, N. M. Muresan, E. Reisner, *Chem. Sci.* **2015**, *6*, 2727 – 2736.
[40] M. A. Nasalevich, R. Becker, E. V. Ramos-Fernandez, S. Castellanos, S. L. Veber, M. V. Fedin, F. Kapteijn, J. N. H. Reek, J. I. van der Vlugt, J. Gascon, *Energy Environ. Sci.* **2015**, *8*, 364 – 375.
[41] A. Le Goff, V. Artero, B. Jousselme, P. D. Tran, N. Guillet, R. Métayé, A. Fihri, S. Palacin, M. Fontecave, *Science* **2009**, *326*, 1384 – 1387.
[42] P. D. Tran, A. Le Goff, J. Heidkamp, B. Jousselme, N. Guillet, S. Palacin, H. Dau, M. Fontecave, V. Artero, *Angew. Chem. Int. Ed.* **2011**, *50*, 1371 – 1374; *Angew. Chem.* **2011**, *123*, 1407 – 1410.
[43] M. A. Gross, A. Reynal, J. R. Durrant, E. Reisner, *J. Am. Chem. Soc.* **2014**, *136*, 356 – 366.
[44] B. Reuillard, J. Warnan, J. J. Leung, D. W. Wakerley, E. Reisner, *Angew. Chem. Int. Ed.* **2016**, *55*, 3952 – 3957; *Angew. Chem.* **2016**, *128*, 4020 – 4025.
[45] R. M. Bullock, A. K. Das, A. M. Appel, *Chem. Eur. J.* **2017**, *23*, 7626 – 7641.
[46] S. Pullen, H. Fei, A. Orthaber, S. M. Cohen, S. Ott, *J. Am. Chem. Soc.* **2013**, *135*, 16997 – 17003.
[47] W. Wang, T. J. Yu, Y. Zeng, J. P. Chen, Y. Li, *Chin. J. Chem.* **2014**, *32*, 479 – 484.
[48] T. J. Yu, Y. Zeng, J. P. Chen, X. H. Zhang, G. Q. Yang, Y. Li, *J. Mater. Chem. A* **2014**, *2*, 20500 – 20505.
[49] S. K. Ibrahim, X. Liu, C. Tard, C. J. Pickett, *Chem. Commun.* **2007**, 1535 – 1537.
[50] P. D. Tran, V. Artero, M. Fontecave, *Energy Environ. Sci.* **2010**, *3*, 727 – 747.
[51] L. J. Antila, P. Ghamgosar, S. Maji, H. Tian, S. Ott, L. Hammarström, *ACS Energy Lett.* **2016**, *1*, 1106 – 1111.
[52] V. Vijaikanth, J. F. Capon, F. Gloaguen, P. Schollhammer, J. Talarmin, *Electrochem. Commun.* **2005**, *7*, 427 – 430.
[53] C. M. Thomas, O. Rüdiger, T. Liu, C. E. Carson, M. B. Hall, M. Y. Darensbourg, *Organometallics* **2007**, *26*, 3976 – 3984.
[54] A. Le Goff, V. Artero, R. Metayé, F. Moggia, B. Jousselme, M. Razavet, P. D. Tran, S. Palacin, M. Fontecave, *Int. J. Hydrogen Energy* **2010**, *35*, 10790 – 10796.
[55] J.-F. Capon, F. Gloaguen, P. Schollhammer, J. Talarmin, *J. Electroanal. Chem.* **2006**, *595*, 47 – 52.
[56] E. S. Donovan, J. J. McCormick, G. S. Nichol, G. A. N. Felton, *Organometallics* **2012**, *31*, 8067 – 8070.
[57] F. Quentel, G. Passard, F. Gloaguen, *Phys. Chem. Chem. Phys.* **2012**, *5*, 7757 – 7761.
[58] F. Quentel, G. Passard, F. Gloaguen, *Chem. Eur. J.* **2012**, *18*, 13473 – 13479.
[59] J. D. Benck, B. A. Pinaud, Y. Gorlin, T. F. Jaramillo, *PLoS One* **2014**, *9*, e107942.
[60] C.-H. Han, S.-D. Han, J. Gwak, S. P. Khatkar, *Mater. Lett.* **2007**, *61*, 1701 – 1703.
[61] S. Roy, V. Pascanu, S. Pullen, G. G. Miera, B. Martin-Matute, S. Ott, *Chem. Commun.* **2017**, *53*, 3257 – 3260.
[62] K. C. Nicolaou, A. A. Estrada, M. Zak, S. H. Lee, B. S. Safina, *Angew. Chem. Int. Ed.* **2005**, *44*, 1378 – 1382; *Angew. Chem.* **2005**, *117*, 1402 – 1406.
[63] H. J. Paul, J. Leddy, *Anal. Chem.* **1995**, *67*, 1661 – 1668.
[64] V. D. Parker, *Acta Chem. Scand.* **1981**, *35*, 259 – 262.
[65] C. Costentin, S. Drouet, M. Robert, J. M. Saveant, *J. Am. Chem. Soc.* **2012**, *134*, 11235 – 11242.
[66] A. L. Eckermann, D. J. Feld, J. A. Shaw, T. J. Meade, *Coord. Chem. Rev.* **2010**, *254*, 1769 – 1802.
[67] As the small hydrogen bubbles were observed to remain trapped at the electrode surface, the bias potential was applied for 5 min. Subsequently the electrodes were gently shaken to liberate the small bubbles, thereafter the headspace was allowed to equilibrate for 30 min before H_2 was quantified.
[68] On the nanostructured FTO, the catalyst loading is about 300 times higher than on the flat electrodes, although the electrolyte refreshment rate would be slower owing to the intrinsic porosity of the material. As such, the combination of these two effects would lead to a more rapid pH change on the nanostructured material and this may lead to quicker decomposition/desorption of the catalyst, explaining the lower TON.

Manuscript received: September 14, 2017
Revised manuscript received: October 26, 2017
Accepted manuscript online: October 27, 2017
Version of record online: December 19, 2017

 © 2018 The Authors. Published by Wiley-VCH Verlag GmbH & Co. KGaA, Weinheim